Unlocking the Lithium Storage Capacity of Aluminum by Molecular Immobilization and Purification

*Guanglin Xia, Hongyu Zhang, Ming Liang, Jian Zhang, Weiwei Sun, Fang Fang, Dalin Sun, and Xuebin Yu**

Aluminum is regarded as a promising alternative for graphite anode in next-generation lithium-ion batteries, but its application is hindered by the simultaneous presence of aluminum oxide and the huge volume changes. Herein, hydrogenation-induced self-assembly of robust Al nanocrystals with high purity that are uniformly anchored on graphene is demonstrated. The strong molecular interaction between Al and graphene can not only thermodynamically facilitate the homogenous distribution of Al on graphene but also effectively alleviate the volume changes and preserve the structural integrity of the electrode. More importantly, density functional theory calculations reveal that the absence of oxidation can lower the energy barrier for Li diffusion inside the Al matrix to less than 1/6 of that in an Al matrix with only one monolayer coverage of oxygen. These unique structural features enable the aluminum/graphene nanosheets (Al@GNs) electrode to realize a high reversible capacity of 1219 mAh g^{-1} and an excellent cycling stability with capacity of 766 mAh g^{-1} after 1000 cycles at the 3 A g^{-1} rate. Furthermore, a full cell, comprising an Al@GNs anode and LiFePO$_4$ cathode, exhibits remarkable capacity retention of 96.4% after 100 cycles at the 0.5 A g^{-1} rate.

Lithium-ion batteries (LIBs) have been predominantly applied in portable electronic devices, but to satisfy the ever-increasing demands for their application in hybrid electric vehicles, electric vehicles, and smart systems, it is of great importance to develop electrode materials with high capacity, long lifespan, and high-rate performance.[1–5] Aluminum (Al) has been especially recognized as an attractive anode material for

next-generation LIBs because of its exceptional capacity of 2235 mAh g^{-1} (formation of Li$_9$Al$_4$), relatively low discharge potential (≈0.19–0.45 V against Li$^+$/Li), high electrical conductivity, and low cost.[6–8] Several essential issues, however, are significantly impeding the practical application of aluminum. The lithium diffusion into the bulk of the Al electrodes and the low diffusion coefficient of lithium in the discharge products, i.e., LiAl alloys, leads to the stripping of lithium and therefore the rapid loss of capacity.[9] Another drawback is the structural pulverization caused by high volume changes during lithiation and delithiation, which results in the continuous formation of an unstable solid electrolyte interphase (SEI) and the loss of electrical contact between the active electrode materials and the current collector, leading to inferior coulombic efficiency and a short battery lifetime.[10] More importantly, Al$_2$O$_3$, which is usually formed during the synthesis procedure, owing to the high activity of Al, is electrochemically inactive with low electrical conductivity, which could cause high electronic resistance and therefore significantly limits the fast transport of lithium ions at high current density.[11]

Fortunately, material nanostructuring, offering a high interfacial area, fast electronic and ionic diffusion, and alleviation of the strain, is a well-established practice to improve the electrochemical properties of high-capacity anode materials, which basically faces the same imperative challenges as the aluminum electrode.[12–17] The building of nanostructures of aluminum, however, is significantly impeded by its special physicochemical properties, i.e., the easy passivation of surfaces and even spontaneous combustion due to its high reactivity, and therefore, the lithium storage behavior of aluminum is still far below the theoretical capacity.[6,11] Up to now, approaches to the synthesis of nanostructured aluminum have only been limited to ball-milling,[18] chemical vapor deposition,[19] and electrodeposition,[20] which normally suffers from inhomogeneous size distributions and severe aggregation with the lack of control over particle size and morphology. On the other hand, it should be noted that nanoparticles (NPs) tend to aggregate to minimize their surface energy induced by volume changes during charge–discharge processes in the course of cycling, leading to fast capacity decay and rather poor cycling life.[21–24] Moreover,

Dr. G. L. Xia, H. Y. Zhang, Prof. F. Fang, Prof. D. L. Sun, Prof. X. B. Yu
Department of Materials Science
Fudan University
Shanghai 200433, China
E-mail: yuxuebin@fudan.edu.cn
M. Liang, Prof. W. W. Sun
Department of Chemical Engineering
School of Environmental and Chemical Engineering
Shanghai University
Shanghai 200444, China
Prof. J. Zhang
Hunan Provincial Key Laboratory of Safety Design and Reliability
Technology for Engineering Vehicles
Changsha University of Science and Technology
Changsha 410114, China

**ADVANCED
SCIENCE NEWS**

www.advancedsciencenews.com
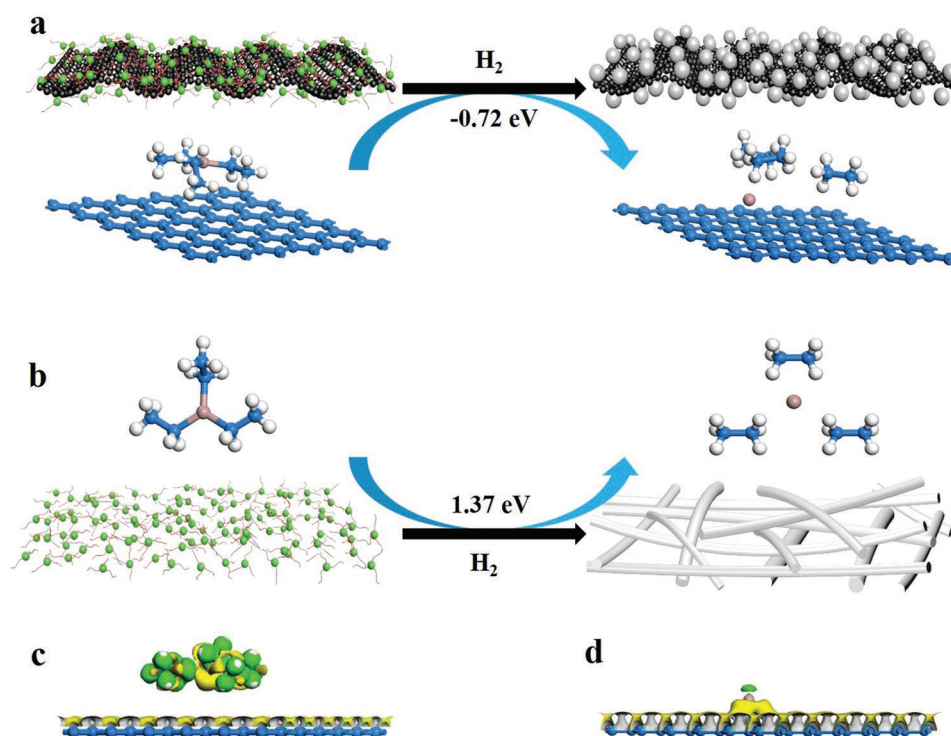
**ADVANCED
MATERIALS**

www.advmat.de

Figure 1. Schematic illustration of a) the synthesis of Al@GNs and b) the synthesis of Al nanofibers (NFs) without the presence of graphene under high-pressure hydrogen, including the calculated reaction enthalpies for the formation of aluminum from the hydrogenation of TEAL with and without the support of graphene, respectively. Relaxed atomic configurations and charge-density-difference isosurfaces of c) TEAL and d) Al (d) on graphene. Blue, white, and pink spheres are C, H, and Al atoms, respectively.

the design of nanostructures could introduce poor overall electrical conduction due to the increased particle interfaces and the induced interparticle resistance, especially when considering the possible formation of Al_2O_3 on surfaces of aluminum nanoparticles.

In order to address these challenging problems, we present the controllable synthesis of Al nanocrystals (NCs), in which Al NCs with an average size of ≈5 nm were homogeneously immobilized and used to form a sandwich structure between layers of graphene nanosheets (with the composite denoted as Al@GNs). First, a hydrogen-induced self-assembly strategy based on the solvothermal reaction of triethylaluminum (TEAL) under the structure-directing effects of graphene was developed to fabricate Al NCs, while the graphene could thermodynamically stabilize the formation of Al clusters, thus promoting the homogenous formation of Al NCs on its surface. More importantly, under the protection of hydrogen, the oxidation of aluminum, which could not only physically block the pathways for Li atom diffusion but also result in more than six times higher energy barriers for the transfer of Li atoms inside the Al matrix, as evidenced by density functional theory (DFT) calculations, could be significantly avoided. The as-synthesized Al NCs with controllable and uniform particle size can offer short diffusion paths for electrons and ions, and large electrode/electrolyte contact areas, which is beneficial to improve the lithium reaction rate. Furthermore, the homogeneous distribution of Al NCs on graphene layers with strong molecular interaction could not only accommodate the volume changes of the Al NCs and prevent their aggregation

during lithiation and delithiation processes, leading to good preservation of their structural stability, but also enhance the conductivity of the whole electrode, leading to a high reversible capacity. With these inspiring advantages of this unique structure, the main challenges to Al-based electrodes could be effectively solved.

The synthesis procedure for Al@GNs is schematically illustrated in **Figure 1**a, in which a hydrogenation-induced solvothermal reaction of TEAL was developed on the surfaces of graphene nanosheets. First-principles calculations based on DFT demonstrate that, under the most stable adsorption configuration, the binding energy between $(C_2H_5)_3Al$ and graphene could reach −0.46 eV (Figure 1c), which is much lower than that between graphene and solvents adopted in the self-assembly process, i.e., the C_7H_{16}-graphene (−0.06 eV) and C_6H_{14}-graphene (−0.03 eV) systems (Figure S1, Supporting Information). Furthermore, the binding energy between Al and graphene could reach −1.72 eV (Figure 1d), indicating the strong electronic interaction between them. The combined favorable adsorption between both precursors and Al and graphene could facilitate the formation of Al clusters on graphene.

After the solvothermal reaction, the X-ray diffraction (XRD) results confirmed the formation of Al with the absence of peaks belonging to aluminum oxide (Figure S2, Supporting Information). Owing to the presence of amorphous tape adopted to avoid the oxidation of Al NCs during XRD measurement, which exhibits strong signals between 20° and 30°, the characteristic peak of graphene at ≈25° was covered up. The chemical composition of Al@GNs was further identified by X-ray photoelectron

**ADVANCED
SCIENCE NEWS**

www.advancedsciencenews.com
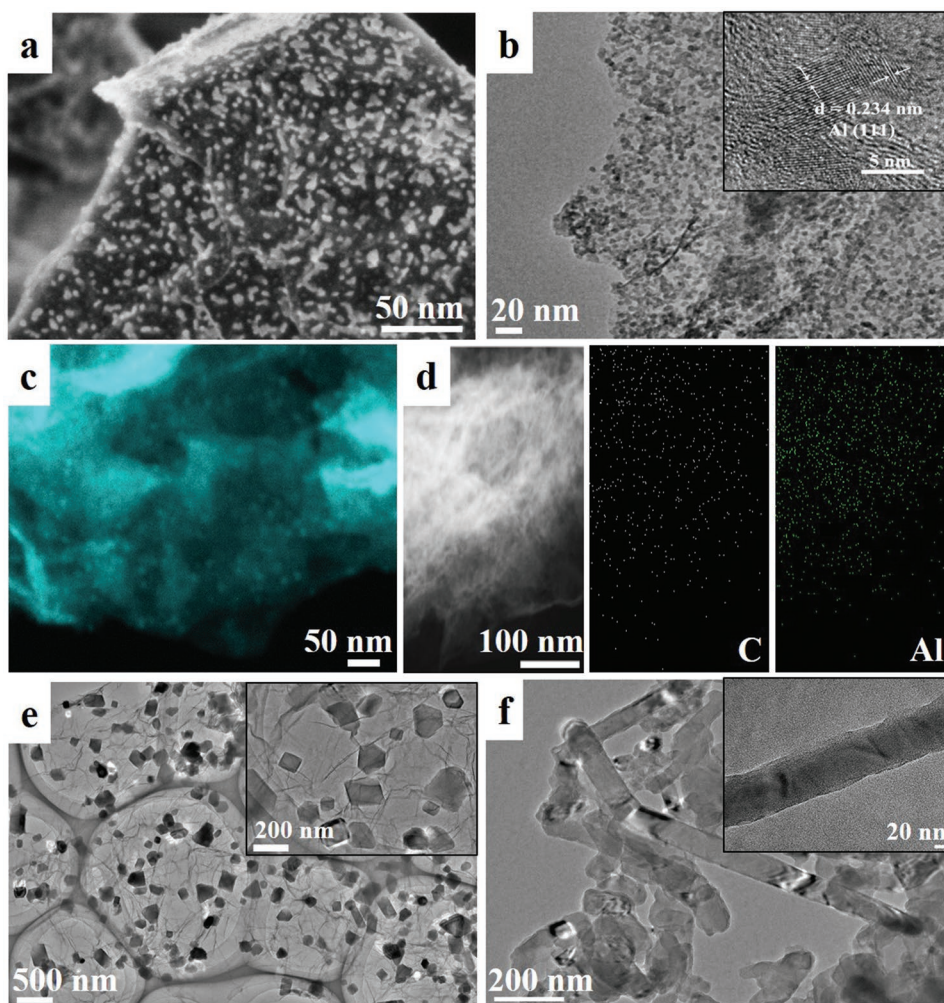
**ADVANCED
MATERIALS**

www.advmat.de

Figure 2. a) SEM, b) TEM (inset: HRTEM image), and c) STEM images of the as-prepared Al@GNs. d) Scanning TEM image of Al@GNs and the corresponding elemental mapping images of carbon (C) and aluminum (Al). Representative TEM images of e) Al@GNs synthesized under argon and f) Al nanofibers synthesized under identical conditions to Al@GNs but without the presence of graphene (inset: magnified image of singles nanofiber).

spectroscopy (XPS), which confirms that only Al and C were present in the hybrid (Figure S3a, Supporting Information), validating the high purity of the as-synthesized aluminum. The high-resolution Al 2p spectrum (Figure S3b, Supporting Information) exhibits a major peak at 73.5 eV that is indexed to metallic Al, with a minor shoulder at 75.3 eV indexed to aluminum oxide.[25] In comparison, although XRD validates the presence of Al in the commercial Al NPs (Figure S1, Supporting Information), only a weak peak indexed to metallic Al could be observed in XPS, with the major peaks belonging to Al_2O_3 in the Al 2p spectrum (Figure S4, Supporting Information), which confirms that commercial Al NPs are usually covered with amorphous aluminum oxide due to their high reactivity.[18] This result provides further evidence of the high-purity of the as-formed Al in Al@GNs. To verify the amount of Al in the hybrid, a hydrolysis reaction between aluminum and sodium hydroxide solution, i.e., $Al + 3H_2O + NaOH \rightarrow NaAl(OH)_4 + 1.5H_2$, was adopted.[26] The results demonstrate that 6.9 mmol hydrogen could be released from 200 mg of Al@GNs (Figure S5, Supporting Information), corresponding to 62% Al in Al@GNs.

The morphology of the as-prepared Al@GNs was further investigated by scanning electron microscopy (SEM) and transmission electron microscopy (TEM) (**Figure 2**), which revealed that Al NCs with an average particle size of ≈ 5.4 nm were anchored on the graphene layers uniformly and densely (Figure S6, Supporting Information). No isolated Al NCs could be observed in TEM measurements of the as-synthesized hybrid after 15 min of sonication, indicating the relatively strong interaction between graphene and aluminum. This favorable interaction could effectively prevent the agglomeration and detachment of Al NCs, preserving the structural integrity of the composite and facilitating the rapid transport of electrons from the graphene to the Al NCs, thus enhancing the electrochemical rate performance. Clear lattice fringes with an interplanar spacing of 0.234 nm, corresponding to the (111) planes of Al, could be observed in the high-resolution TEM (HRTEM) image, in good agreement with the XRD results. Moreover, the scanning TEM (STEM) image (Figure 2c) verifies the presence of spaces between individual Al NCs, which could effectively improve the lithium ion diffusion into the

**ADVANCED
SCIENCE NEWS**

www.advancedsciencenews.com

**ADVANCED
MATERIALS**

www.advmat.de

Al NCs and accommodate the volume changes of the Al NCs during lithiation and delithiation processes in the course of cycling. The elemental mapping (Figure 2d) demonstrates that the Al and C elements are evenly distributed throughout the whole composite, which further confirms the homogenous distribution of Al NCs on the graphene nanosheets. In strong contrast, large particles with various shapes and sizes ranging from 50 to 300 nm are formed on graphene without the presence of hydrogen (Figure 2e), and more interestingly, only Al nanofibers with an average diameter of around 56 nm are synthesized in the absence of graphene (Figure 2f). This indicates that both hydrogen and graphene play an important role in facilitating the homogeneous nucleation and formation of Al NCs (Figure S7, Supporting Information). With the optimized geometry, it is demonstrated that, with the support of graphene, the lengths of Al−C bonds in TEAL are increased (Figure S8, Supporting Information), and a clear overlap between Al atoms and graphene could be observed with a charge transfer of 0.44 e from Al to graphene (Figure 1d). This confirms that graphene

could weaken the Al−C bonds of TEAL and, on the other hand, stabilize the formation of Al. As a result, the energy required for the formation of Al from the hydrogenation of TEAL is significantly decreased to −0.72 eV in the presence of graphene, much lower than the value (1.37 eV) without the presence of graphene. These results directly demonstrate that graphene could thermodynamically facilitate the formation of Al clusters, which, coupled with the favorable adsorption of TEAL and Al on graphene, could contribute to the controllable synthesis of Al NCs on graphene in a homogenous distribution.

The electrochemical performance of the as-prepared Al@GNs was first evaluated using lithium foil as the counter electrode in coin cells. **Figure 3**a shows the cyclic voltammetry (CV) curves of the Al@GNs electrode at a scanning rate of 0.1 mV s^{-1}. In the first cathodic scan, a broad irreversible peak occurs at around 0.76 V, but it disappears in the subsequent cycles, which could be attributed to the formation of the solid-electrolyte interphase (SEI) film. In addition, there are two sharp reductive peaks at around 0.21 and 0.05 V, corresponding
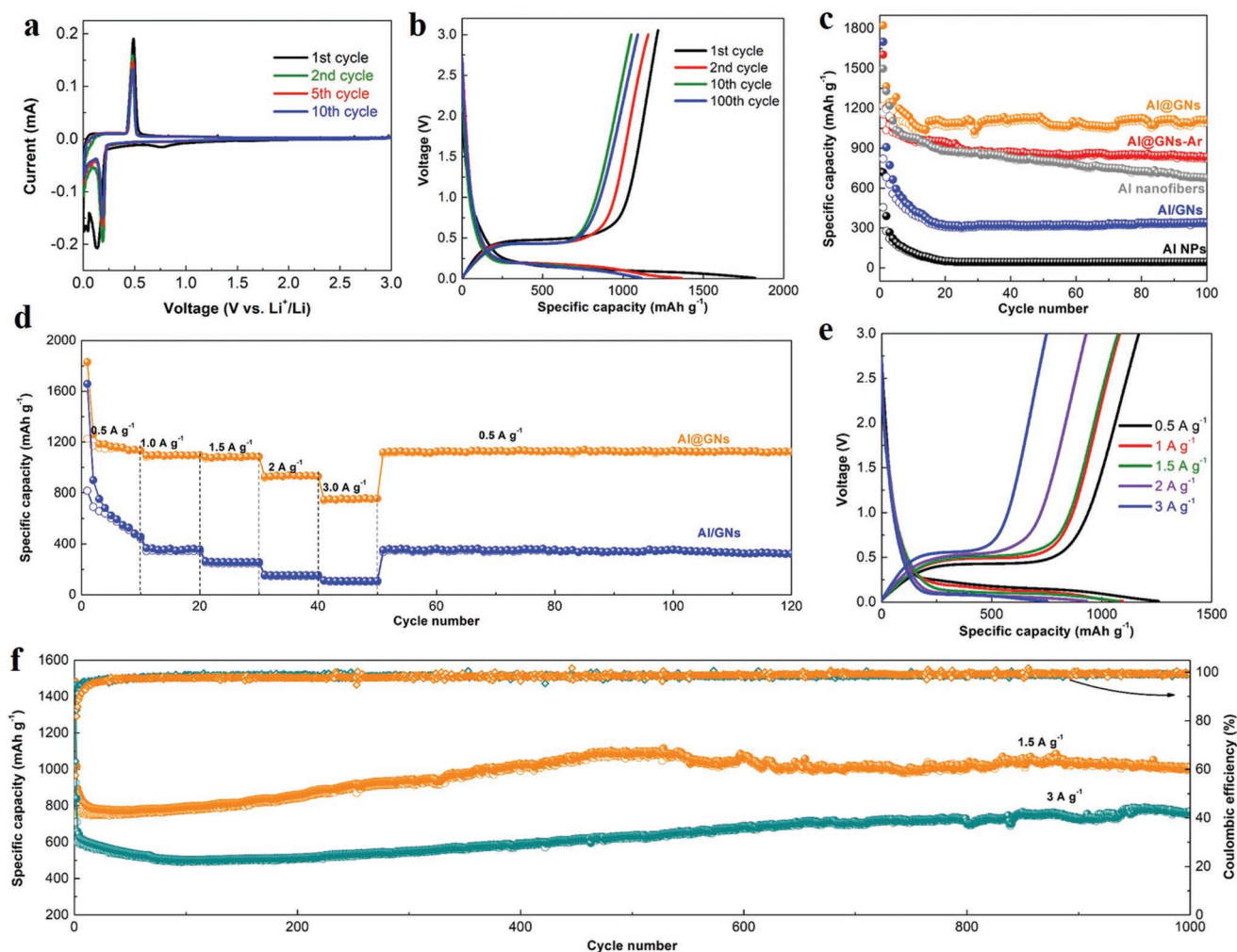

Figure 3. Electrochemical performance of the Al@GNs electrode in LIBs. a) Cyclic voltammograms from the initial ten cycles of the Al@GNs electrode at a scanning rate of 0.1 mV s^{-1}. b) Galvanostatic discharge–charge profiles for selected cycles at 0.5 A g^{-1}. c) Cycling performance at 0.5 A g^{-1} of Al@GNs electrode, with Al@GNs-Ar, Al nanofibers, Al NPs, and Al/GNs included for comparison. d) Rate performance of Al@GNs electrode, with its potential profiles presented in (e). f) Cycling performance of Al@GNs electrode at 1.5 and 3 A g^{-1}.

to the alloying reaction between Al and Li$^+$.[6] Only one peak near 0.48 V was observed in the anodic scan from the first to the tenth cycle, which could be ascribed to the dealloying of the Li–Al alloys.[11] The high superposition of peaks in terms of sharpness, intensity, and potential position in the following cycles suggests excellent electrochemical reaction reversibility.

The voltage versus discharge–charge capacity profiles of the first, second, tenth, and 100th cycles at 0.5 A g^{-1} between 0.005 and 3.0 V are shown in Figure 3b. All the voltage plateaus in the discharge and charge curves of Al@GNs correspond well with the reductive and oxidative peaks in the CV curves. The discharge and charge plateaus are well preserved after 100 cycles, suggesting stable electrochemical reactions of the graphene-supported Al NCs. The initial specific discharge and charge capacities of Al@GNs approach 1823 and 1219 mAh g^{-1}, respectively, corresponding to an initial Coulombic efficiency (CE) of 67%. It should be noted that all specific capacities of Al@GNs in half-cells were calculated based on the total weight of Al@GNs. The initial capacity loss is attributed to the irreversible decomposition of the electrolyte, leading to the formation of SEI films on the surfaces of electrodes. By comparison, the initial discharge capacities of Al@GNs synthesized under argon (denoted as Al@GNs-Ar) and Al nanofibers were only 1604 and 1498 mAh g^{-1}, respectively, which is mainly attributed to their large particle size compared with Al@GNs (Figure 2). After that, the specific charge capacity of Al@GNs slowly decayed from 1158 to 1093 mAh g^{-1} from the second to the 100th cycle, corresponding to a capacity retention of 94.4%. In strong contrast, both the commercial Al NPs and the mechanically milled composite of Al NPs and graphene (denoted as Al/GNs) exhibited much lower reversible charge and discharge capacities and suffered from rapid capacity fading (Figure S9, Supporting Information). The initial CE of Al NPs was 64%, and, with the addition of GNs into Al NPs to form Al/GNs, the initial CE was decreased to 48%. It indirectly confirms that, combined with the fact that an initial CE of only 32% was observed for pure GNs (Figure S10, Supporting Information), the low initial CE of Al@GNs could be mainly induced by the presence of graphene. In addition, it is interesting to notice that a reversible capacity of 837 mAh g^{-1} could be achieved for Al@GNs-Ar after 100 cycles, while the reversible capacities of Al nanofibers decayed to only 678 mAh g^{-1}, which directly demonstrates the structural support role of graphene could effectively alleviate the volume change of Al upon cycling lithiation and delithiation process. Therefore, it is concluded that the electrochemical performance of Al@GNs is much superior to both Al@GNs-Ar and Al nanofibers and Al NPs and Al/GNs, which could be attributed to the uniform particle size and homogeneous distribution of Al NPs on the graphene, the electronic conductivity of graphene, and the favorable electronic interaction between them. Furthermore, the effect of loading ratio of Al in Al@GNs on their lithium storage performance was subsequently investigated. As shown in Figure S11 in the Supporting Information, with the increase of loading ratio of Al from 62% to 73%, although the initial specific capacities of Al@GNs increased due to the increasing amount of active materials for lithium storage, the reversible capacities rapidly decayed to 975 mAh g^{-1}. This result could be attributed to the possible agglomeration and growth of Al NCs with higher

density and less interparticle distance induced by the increase of loading ratio. By comparison, with the decrease of loading ratio of Al to 51%, only a reversible capacity of 918 mAh g^{-1}, although with superior cycling stability, could be achieved after 100 cycles. Therefore, considering both the specific capacities and the cycling stability, Al@GNs with an optimal loading amount of 62% was selected for detailed investigation.

The rate performance is another critical concern for practical applications of LIBs, such as in the commercial production of electric cars.[27–32] Excitingly, the graphene-supported Al NCs exhibit an outstanding rate performance, delivering an average reversible capacity of 1172 mAh g^{-1} at 0.5 A g^{-1} (Figure 3d). Even when the current density was increased to 3 A g^{-1}, a reversible capacity of around 756 mAh g^{-1} could be achieved. By comparison, the capacity of Al/GNs rapidly decreased to only 110 mAh g^{-1} at 3 A g^{-1}. More importantly, if the current density was returned to 0.5 A g^{-1} after cycling under high current densities, the Al@GNs could still retain a reversible capacity near 1128 mAh g^{-1}, corresponding to a capacity retention of 96.2%, which validates the strong tolerance of Al@GNs towards fast lithium ion insertion and extraction. The representative charge/discharge profiles of Al@GNs electrode at various current densities (Figure 3e) illustrate its highly reversible electrochemical behavior with only slightly increased overpotentials at high current rates.

The cycling performance of Al@GNs electrode was further evaluated at 1.5 and 3 A g^{-1} (Figure 3f). The discharge and charge capacity of the electrode reaches 1011 and 766 mAh g^{-1}, respectively, after 1000 cycles, corresponding to high capacity retention of 99.4% and 91.2% compared to the specific capacity of the second cycle. The difference of reversible capacities at different current densities is mainly attributed to the fact that, with the increase of current densities, losses of capacities increase resulting from the presence of an intrinsic internal resistance[33] and the presence of kinetic limitations resulting from the slow solid-state charge diffusion and transfer processes in the electrodes results in the decreased utilization ratio of active Al@GNs.[34,35] More importantly, CEs of over 97% are well maintained through the whole cycling process, providing further evidence of the good reversibility of its electrochemical reactions and the formation of stable SEI films. After 200 cycles of discharge–charge processes, the layered structure of Al@GNs is well maintained (Figure S12a, Supporting Information), and the good distribution of Al NCs is confirmed by energy dispersive spectroscopy elemental mapping (Figure S13, Supporting Information), which demonstrates that the homogeneous distribution of Al NCs in Al@GNs electrode is well preserved after cycling. This suggests the molecular immobilization of Al by graphene, which, coupled with the minimized lithiation/delithiation stresses from homogeneous Al NCs and the structural support of graphene, could space-confine Al NCs and prevent them from peeling off from the graphene nanosheets during cycling. HRTEM confirms the formation of LiAl and Li$_9$Al$_4$ alloys during the lithiation process (Figure S12c, Supporting Information) and the regeneration of Al during the reverse delithiation process (Figure S12d, Supporting Information), indicating the stable reversibility of Al@GNs as electrode material in LIBs.

**ADVANCED
SCIENCE NEWS**

www.advancedsciencenews.com

**ADVANCED
MATERIALS**

www.advmat.de

Electrochemical impedance spectroscopy (EIS) was further performed to understand the cycling performance of Al@GNs electrode (Figure S14, Supporting Information). All EIS spectra consists of a compressed semicircle in the high-to-medium frequency region, corresponding to the charge transfer resistance (R_{ct}), and an inclined straight line in the low-frequency region, corresponding to typical Warburg behavior associated with Li⁺ diffusion within the electrode. Based on the fitting results according to the equivalent circuit model (Figure S15, Supporting Information), Al@GNs displayed an R_{ct} of 114.8 Ω before cycling, which is much lower than that of the Al/GNs (192.3 Ω). The homogeneous contact between the highly conductive graphene and the high purity of the as-synthesized Al NCs could facilitate electron transfer from the anchored Al NCs throughout the whole electrode and thus decrease the resistance. Due to the formation of unstable SEI film and the tremendous volume changes during cycling, the corresponding value for Al/GNs increased to 221.6 Ω after 200 cycles, which coincides with its large capacity decay. In strong contrast, the charge transfer resistance of Al@GNs exhibits only a slight reduction to 61.5 Ω, which suggests the formation of a stable SEI film and an activation process during cycling. This result provides further evidence of the excellent cycling stability of Al@GNs owing to its well-preserved electronic conductivity under continuous charge–discharge cycling.

In addition to the above well-known structural factors for boosting the electrochemical performance of Al, DFT calculations were implemented to better understand the mechanism behind the improvement of Al@GNs as LIB anode material from lithium adsorption to diffusion. First, the adsorption of Li atoms on pristine Al clusters supported on graphene was examined, which revealed that the energy required for the adsorption of 1 and 6 Li atoms is significantly decreased to −2.697 and −14.340 eV for Al clusters on graphene, respectively, much lower than that on pristine clusters alone (**Figure 4**a,b). Mulliken charge analysis (Figure S16, Supporting Information) revealed that, due to the favorable charge transfer between graphene and Al clusters, graphene contributes to the charge transfer capability from Li to Al clusters to a large extent, and hence, the adsorption of Li on Al clusters supported on graphene is greatly enhanced relative to pristine Al clusters, which favors the fast lithium storage process of Al.

Second, DFT calculations demonstrated that the Li migration barrier on the clean Al (111) surface is around 0.73 eV. In comparison, the effective energy barrier for lithium diffusion from the surface to the third Al layer (Figure 4c) significantly increases to 2.95 and 4.48 eV with an oxygen coverage of 1/2 and 1 monolayer (ML), respectively, being four times and six times more than that on a clean Al (111) surface. This result identifies the negative role of the easy oxidation of Al, leading
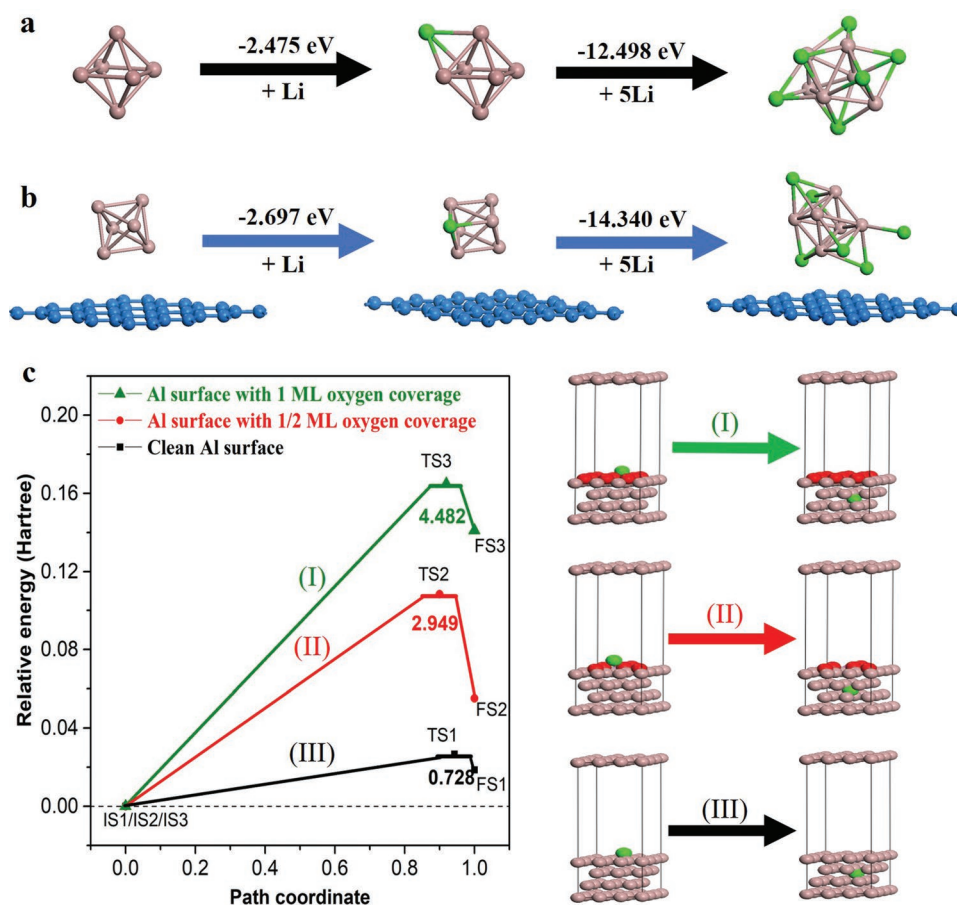

Figure 4. The lithium adsorption energy on Al clusters a) without and b) with the support of graphene. c) Diffusion of lithium atom in the clean Al (111) surface in comparison with Al (111) surfaces with an oxygen coverage of 1/2 monolayer (ML) and 1 ML, respectively.

ADVANCED
SCIENCE NEWS
www.advancedsciencenews.com

ADVANCED
MATERIALS
www.advmat.de

to the formation of Al_2O_3, which could not only physically block the pathways for Li atom diffusion but also result in high energy barriers against the transfer of Li atoms inside the Al matrix, thus attenuating the electrochemical activity of Al. As a result, it is remarkably interesting to note that the electrochemical performance of Al@GNs is significantly degraded even after partial oxidation with a weight percent of only ≈10% (Figure S17, Supporting Information). Thus, these combined theoretical and experimental results clearly demonstrate the synergistic effect of graphene and the formation of uniform Al NCs with high purity plays a vital role in promoting the electrochemical performance of aluminum anode, while the strong interaction between graphene and Al enables the structural integrity of the whole electrode, leading to excellent cycling stability. Such superior electrochemical properties of Al@GNs are among the best of Al-based anode materials and compare favorably to the state-of-art values reported for Si-based anode materials (Figure S18 and Table S1, Supporting Information).

For proof-of-concept, we further investigated the potential practical applications of Al@GNs by assembling full LIBs with commercial $LiFePO_4$ (LFP). Since the operating potential of LFP and Al@GNs after activation is respectively 3.4 and 0.45 V versus Li/Li$^+$ (**Figure 5**a), the full cell battery gives an average discharge voltage of around 2.87 V (Figure 5b). The full LIB

delivers a high discharge capacity of 133 mAh g^{-1} based on the total mass of Al@GNs and LFP within the voltage window of 2.3 and 3.7 V, with an impressive energy density of 382 Wh kg^{-1} at 100 mA g^{-1}. Even at the high current density of 500 mA g^{-1}, the Al@GNs//LFP full cell could achieve a reversible capacity of 112 mAh g^{-1}, and the discharge capacity is able to recover to 130 mAh g^{-1} when the rate returns to 100 mA g^{-1}, indicating the high reversibility of Al@GNs. The Al@GNs//LFP full cell also exhibited excellent cycling stability, and the discharge capacity was maintained at 108 mAh g^{-1} even after 100 cycles, with a capacity retention ratio of 96.4%. Furthermore, the fabricated coin cells could power commercial blue light-emitting diodes (LEDs) with a working voltage of 2.2 and 2.4 V (inset of Figure 5d), which demonstrates the stable working voltage of the full cell, indicating the promising application of Al@GNs as a high-performance anode material for LIBs.

In conclusion, a novel hydrogen-induced assembly strategy has been developed to fabricate Al NCs with high purity that are homogenously anchored on graphene nanosheets. The strong molecular interaction between TEAL and Al and graphene could not only thermodynamically enable the homogeneous formation of Al NCs on graphene but also preserves structural integrity during the synthesis of Al@GNs, enabling it to withstand repeated lithiation and delithiation cycles. Coupled with
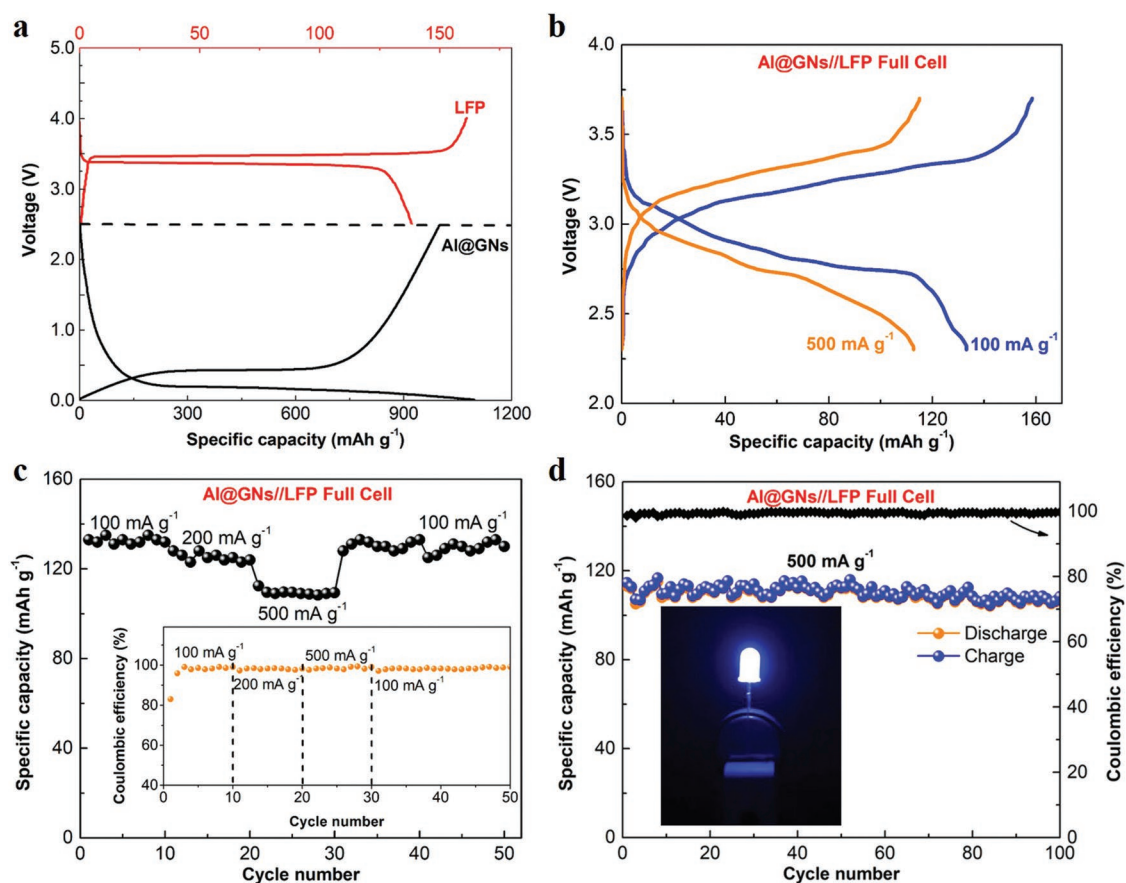

Figure 5. Energy storage performance of the Al@GNs@LFP full cells. a) Galvanostatic discharge–charge profiles for commercial LFP and Al@GNs half cells. b) Galvanostatic discharge–charge profiles at 100 and 500 mA g^{-1}, c) rate capability (inset: Coulombic efficiency), and d) cycling performance at 500 mA g^{-1} of full cells (inset: blue LED powered by a full cell).

the unique structural features of Al@GNs, which consists of ultrafine Al NCs uniformly and molecularly immobilized on the GNs, the Al@GNs electrode exhibits ultralong cycle life, high reversible capacity, and high rate capability. Our experimental results are well corroborated by the DFT calculations, which reveal that not only could graphene facilitate Li adsorption on Al clusters but also the absence of oxidation could effectively reduce the energy barriers for Li diffusion inside the Al matrix. This is good evidence that our work could open up new opportunities towards realizing the practical application of Al-based electrode materials and that the present strategy may be extended to the fabrication of various nanostructured Al-based functional materials for wide applications.

Supporting Information

Supporting Information is available from the Wiley Online Library or from the author.

Conflict of Interest

The authors declare no conflict of interest.

[1] Y. Sun, N. Liu, Y. Cui, *Nat. Energy* **2016**, *1*, 16071.

[2] S. Chen, L. Shen, P. A. van Aken, J. Maier, Y. Yu, *Adv. Mater.* **2017**, *29*, 1605650.

[3] M. R. Lukatskaya, B. Dunn, Y. Gogotsi, *Nat. Commun.* **2016**, *7*, 12647.

[4] B. Dunn, H. Kamath, J.-M. Tarascon, *Science* **2011**, *334*, 928.

[5] M. Li, J. Lu, Z. Chen, K. Amine, *Adv. Mater.* **2018**, *30*, 1800561.

[6] Z. Li, J. T. Zhang, Y. M. Chen, J. Li, X. W. Lou, *Nat. Commun.* **2015**, *6*, 8850.

[7] M. J. Lindsay, G. X. Wang, H. K. Liu, *J. Power Sources* **2003**, *119–121*, 84.

[8] Y. Hamon, T. Brousse, F. Jousse, P. Topart, P. Buvat, D. M. Schleich, *J. Power Sources* **2001**, *97–98*, 185.

[9] D. X. Liu, A. C. Co, *J. Am. Chem. Soc.* **2016**, *138*, 231.

[10] Y. Liu, N. S. Hudak, D. L. Huber, S. J. Limmer, J. P. Sullivan, J. Y. Huang, *Nano Lett.* **2011**, *11*, 4188.

[11] X. Chang, Z. Xie, Z. Liu, X. Zheng, J. Zheng, X. Li, *Nano Energy* **2017**, *41*, 731.

[12] X.-Y. Yu, L. Yu, X. W. Lou, *Adv. Energy Mater.* **2016**, *6*, 1501333.

[13] Y. Zhao, X. Li, B. Yan, D. Xiong, D. Li, S. Lawes, X. Sun, *Adv. Energy Mater.* **2016**, *6*, 1502175.

[14] G. Chen, L. Yan, H. Luo, S. Guo, *Adv. Mater.* **2016**, *28*, 7580.

[15] C. Yuan, H. B. Wu, Y. Xie, X. W. Lou, *Angew. Chem., Int. Ed.* **2014**, *53*, 1488.

[16] Y. Wen, Y. Zhu, A. Langrock, A. Manivannan, S. H. Ehrman, C. Wang, *Small* **2013**, *9*, 2810.

[17] L. Peng, Y. Zhu, D. Chen, R. S. Ruoff, G. Yu, *Adv. Energy Mater.* **2016**, *6*, 1600025.

[18] B. W. McMahon, J. Yu, J. A. Boatz, S. L. Anderson, *ACS Appl. Mater. Interfaces* **2015**, *7*, 16101.

[19] J. Benson, S. Boukhalfa, A. Magasinski, A. Kvit, G. Yushin, *ACS Nano* **2012**, *6*, 118.

[20] C.-J. Su, Y.-T. Hsieh, C.-C. Chen, I. W. Sun, *Electrochem. Commun.* **2013**, *34*, 170.

[21] X. Xu, J. Liu, Z. Liu, J. Shen, R. Hu, J. Liu, L. Ouyang, L. Zhang, M. Zhu, *ACS Nano* **2017**, *11*, 9033.

[22] Z. Liu, X.-Y. Yu, U. Paik, *Adv. Energy Mater.* **2016**, *6*, 1502318.

[23] S. Wu, R. Xu, M. Lu, R. Ge, J. Iocozzia, C. Han, B. Jiang, Z. Lin, *Adv. Energy Mater.* **2015**, *5*, 1500400.

[24] G. L. Xia, L. Zhang, F. Fang, D. Sun, Z. Guo, H. Liu, X. B. Yu, *Adv. Funct. Mater.* **2016**, *26*, 6188.

[25] J. O. M. Bockris, Y. Kang, *J. Solid State Electrochem.* **1997**, *1*, 17.

[26] V. Shmelev, V. Nikolaev, J. H. Lee, C. Yim, *Int. J. Hydrogen Energy* **2016**, *41*, 16664.

[27] N.-S. Choi, Z. Chen, S. A. Freunberger, X. Ji, Y.-K. Sun, K. Amine, G. Yushin, L. F. Nazar, J. Cho, P. G. Bruce, *Angew. Chem., Int. Ed.* **2012**, *51*, 9994.

[28] Y. Lu, L. Yu, X. W. Lou, *Chem* **2018**, *4*, 972.

[29] J. Lu, T. Wu, K. Amine, *Nat. Energy* **2017**, *2*, 17011.

[30] Y. Tang, Y. Zhang, W. Li, B. Ma, X. Chen, *Chem. Soc. Rev.* **2015**, *44*, 5926.

[31] W. Li, B. Song, A. Manthiram, *Chem. Soc. Rev.* **2017**, *46*, 3006.

[32] L. Croguennec, M. R. Palacin, *J. Am. Chem. Soc.* **2015**, *137*, 3140.

[33] M. R. Palacín, A. de Guibert, *Science* **2016**, *351*, 1253292.

[34] J. B. Goodenough, K. S. Park, *J. Am. Chem. Soc.* **2013**, *135*, 1167.

[35] Y. X. Tang, Y. Y. Zhang, W. Li, B. Ma, X. D. Chen, *Chem. Soc. Rev.* **2015**, *44*, 5926.